Applied Surface Science 586 (2022) 152641

Contents lists available at ScienceDirect

Applied Surface Science

journal homepage: www.elsevier.com/locate/apsusc

Full Length Article

Unveiling the structural, electronic, and optical effects of carbon-doping on multi-layer anatase TiO_2 (101) and the impact on photocatalysis

Nur Umisyuhada Mohd Nor [a], Elham Mazalan [b], Chad Risko [c], Mark Crocker [c], Nor Aishah Saidina Amin [a,*]

[a] Chemical Reaction Engineering Group (CREG), School of Chemical and Energy Engineering, Faculty of Engineering, Universiti Teknologi Malaysia (UTM), 81310 Johor, Malaysia
[b] Department of Physics, Faculty of Science, Universiti Teknologi Malaysia (UTM), 81310 Johor, Malaysia
[c] Department of Chemistry and Center for Applied Energy Research (CAER), University of Kentucky, Lexington, KY 40506, USA

ARTICLE INFO

Keywords:
C-doped TiO_2
Defects
Photocatalysis
Anatase
DFT
Sub-surface

ABSTRACT

Carbon-doped (C-doped) TiO_2 has demonstrated effective photocatalytic activity in the visible-light region. Here, we make use of density functional theory (DFT) methods to understand the photocatalytic activity of C-doped anatase-TiO_2 (101) surfaces as a function of layer thickness. The formation energy results show that C-doped O sites (C_O) are more stable in the bulk than in the subsurface or on the surface, while C-doped Ti sites (C_{Ti}) are more stable on the surface than in the bulk or subsurface. C_O defects introduce impurity states in the band gap, do not affect the band gap energy, and induce an electron trap close to the conduction band edge and enhances light absorption in the visible and IR spectrum. C_{Ti} defects induce structural distortions caused by a C—O covalent bond with no impurity states formed in the band gap although there is a reduction in the band gap energy, which leads to a red-shifted absorption. These results shed insight on how carbon doping influences the electronic and optical properties of anatase that can be implemented in the design of semiconductor materials with high photocatalytic activity.

1. Introduction

Among the various titanium dioxide (TiO_2) polymorphs, the anatase polymorph has gained considerable interest due to its affordable, stability, recyclability, and photocatalytic activity [1,2]. Hence, anatase TiO_2 (a-TiO_2) has been widely used in various applications, including sensing, optical devices, and solar cells [3]. However, the large band gap (3.2 eV; i.e., absorption only in UV region of the solar spectrum) and fast recombination of photo-generated electron-hole pairs have limited wide adoption in photocatalysis. Approaches to overcome these challenges include doping TiO_2 with metals and non-metals [4-7]. Unfortunately, the performance of modified TiO_2 with metal dopants suffers due to poor thermal stability and photo-corrosion [8]. For non-metal dopants, nitrogen [9], carbon [10], fluorine [11], sulphur [12] and iodine [13] have been evaluated. Carbon-doped (C-doped) TiO_2, in particular, has shown promise as photocatalyst due to enhanced photoactivity and ability to supress the recombination of electron-hole pairs [14] and has ability to absorb light in visible region [15]. Hence, C-doped TiO_2 has been used widely as a photocatalyst for aqueous pollution degradation [16].

The structure of C-doped TiO_2 also influences the physicochemical properties of TiO_2, by substitutional atom replacement in the host semiconductor material. The enhanced photocatalytic performance of C-doped TiO_2 composites has been attributed to both the porous nature of the carbon supports and the strong electronic interaction between the two components. Theoretical investigations on the effect of carbon-doping on the optoelectronic properties of TiO_2 have been undertaken [16,17]. In particular, density functional theory (DFT) methods have been used to investigate how bulk C-doped anatase TiO_2 affects the electronic structure, band gap, charge density, defect formation energy, and optical properties [18-20]. Heffner et. al., investigated substitutional C@Ti and C@O doped brookite TiO_2 (bulk phase) on the structural, electronic and optical properties [20]. Gao et. al. investigated the characteristics of C-doped TiO_2 with three different oxidation states [21]. The electronic structure of C and S doped of the (101) anatase TiO_2 surface and bulk, focusing on a comparison of the computational and experimental optical properties, has also been completed [22]. Some studies have discussed the relationship of surface TiO_2 to the molecules such as H_2O and O_2 by theoretical study DFT [23,24].

* Corresponding author.
E-mail address: noraishah@cheme.utm.my (N.A.S. Amin).

https://doi.org/10.1016/j.apsusc.2022.152641
Received 13 October 2021; Received in revised form 24 January 2022; Accepted 25 January 2022
Available online 5 February 2022

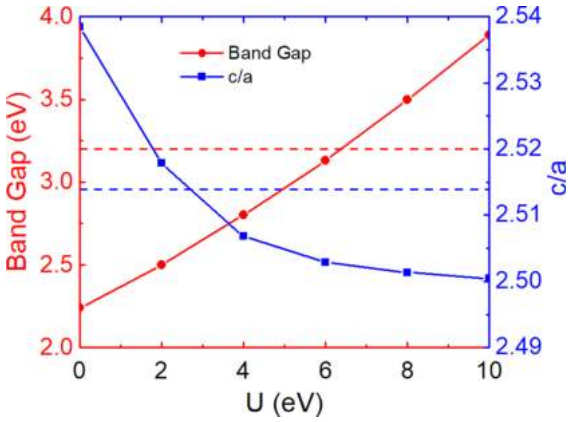

Fig. 1. Band gap and c/a of pristine a-TiO_2 bulk calculated as the Hubbard U parameter varies. The red and blue dashed line represent experimental values for band gap and c/a, respectively. (For interpretation of the references to colour in this figure legend, the reader is referred to the web version of this article.)

Notably, many of these theoretical studies provide different explanations regarding the enhancement of TiO_2 photoactivity. Therefore, studies comparing defect properties of surface, subsurface, and bulk structures are important for filling the gaps relating computational chemistry and photocatalytic activity.

In this work we model a (1 0 1) surface slab of a-TiO_2 since it is the most stable and commonly exposed surface [25]. The objective of the present work is to identify how carbon dopants on the (1 0 1) surface, in the subsurface, and in the bulk affects the electronic and optical properties. Spin-polarized DFT methods were utilized to determine the density of states, band structures, overlap populations, charge densities, and absorption spectra of pristine, C-doped O sites (C_O), and C-doped Ti sites (C_{Ti}). The results demonstrate how these different doping sites influence critical properties that could affect the overall photocatalytic characteristics of anatase TiO_2.

2. Computational methods

Spin-polarized density functional theory (DFT) calculations with projector-augmented wave (PAW) potentials [26] were carried out with the VASP software suite [27]. The PBEsol exchange correlational function was used for geometry optimizations [28], while the electronic structures and optical properties were evaluated with the Perdew-Burke-Ernzerhof (PBE) functional [29]. The configuration of core and valence electrons was treated as Ti ($3p^6 3d^3 4s^1$), O ($2s^2 2p^4$), and C ($2s^2 2p^2$). For the plane-wave basis, the energy cut-off was fixed at 500 eV. All the atoms were fully relaxed with maximum force set at 0.02 eVÅ^{-1}. Brillouin-zone (BZ) integrations were carried out using Γ-centered Monkhorst–Pack grids of 5 × 5 × 1 k-points mesh for ionic relaxations, and 10 × 10 × 1 k-points mesh for electronic and optical calculations.

Due to the underestimated band gap and delocalization error of 3d-states of titanium, the Hubbard U [30] method was implemented to overcome the problems at reduced computational cost. The strategy for choosing a suitable value for the U parameter was by optimizing the pristine bulk anatase parameter and then correlating the experimental and theoretical results [31]. We considered carefully the impact of the U parameters, on both the geometric and electronic structures in order to keep the percentage error small between the theoretical and experimental values. These characteristics are, of course, difficult to deconvolute, especially when there are multiple types of bonding interactions possible in the system. Given this difficulty, we followed established protocols as described in [32] and [20]. For obtaining predicted results that best fit with experimental values, the U parameter was adjusted by comparing the computed band gap and lattice parameter ratio, c/a, of pristine a-TiO_2 bulk to earlier studies [33,34].

The calculated band gaps and structural properties of a pristine a-TiO_2 bulk with varying U are shown in Fig. 1, with the optimized band gap value obtained at U = 6.40 eV and the best match for the c/a obtained at U = 2.97 eV. Thus, in order to achieve a balance of optical and structural performance, U = 5.20 was chosen for the Hubbard U. In comparison to Hubbard U of 5.20 eV, the band gap of pristine a-TiO_2 bulk and pristine a-TiO_2 (1 0 1) is 3.00 eV and 3.17 eV, respectively. A larger band gap is observed on the surface compared to the bulk, which is in good agreement with the previous theoretical study [35]. A comparison of electronic structure of pristine a-TiO_2 (1 0 1) for standard DFT and DFT + U for U of 5.2 eV and 6.4 eV, as shown in Figure S1.

Slabs consisting of four TiO_2 layers comprising 120 atoms and a vacuum layer with a thickness of 15 Å were constructed to simulate characteristics of the (1 0 1) anatase TiO_2 surface, referred to hereafter as a-TiO_2 (1 0 1). A 2 × 2 supercell surface was modelled using periodic boundary conditions on the x-y plane. The bulk region of a-TiO_2 (1 0 1) is composed of 3-fold coordinated oxygen (vertically as in Fig. 2(a) and side-by-side as in Fig. 2(b)) and 6-fold coordinated titanium (Fig. 2(c)), whereas the surface consists of 2-fold coordinated oxygen with removed Ti_3 as in Fig. 2 (a), 3-fold coordinated oxygen as in Fig. 2 (b), and 5-fold coordinated titanium with removed O_6 as in Fig. 2 (c) [36]. The substitution of one carbon atom for either one titanium or oxygen atom at all possible sites (C_{O_bulk}, C_{O_sub}, $C_{O\_surf\text{-}2f}$, $C_{O\_surf\text{-}3f}$, C_{Ti_bulk}, C_{Ti_sub}, and C_{Ti_surf}) mentioned in Fig. 1(d) at the bulk, subsurface, and surface was considered to investigate defects. This corresponds to a defect concentration of 0.83% carbon on a-TiO_2 (1 0 1). In subsurface and surface

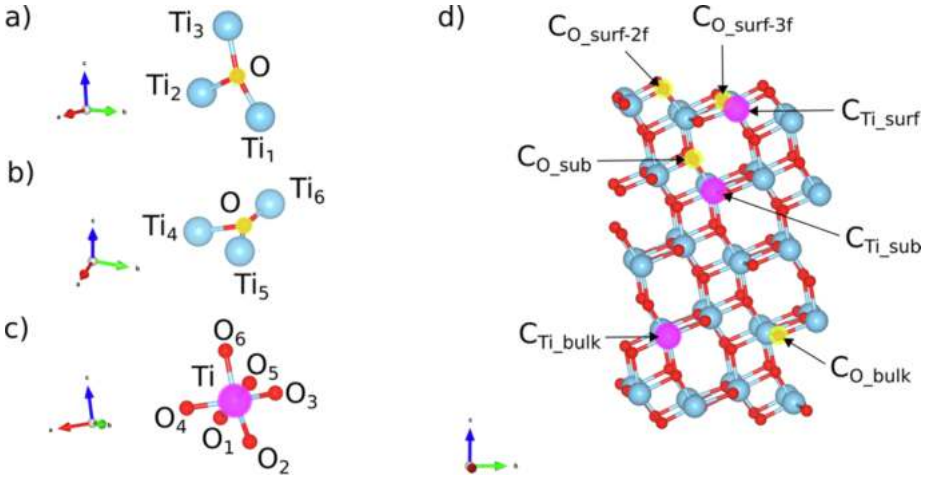

Fig. 2. Types of Ti-O bonding configuration that exist to build the block structure of a-TiO2 (a-c). (d) Atom coordination and labelling for selected arrangements in a-TiO_2 (1 0 1) slab and targeted site for substitutional carbon doping. The blue and red spheres represent titanium and oxygen, respectively, while the magenta and yellow highlights correspond potential sites for carbon substitutional doping of titanium and oxygen, respectively. (For interpretation of the references to colour in this figure legend, the reader is referred to the web version of this article.)

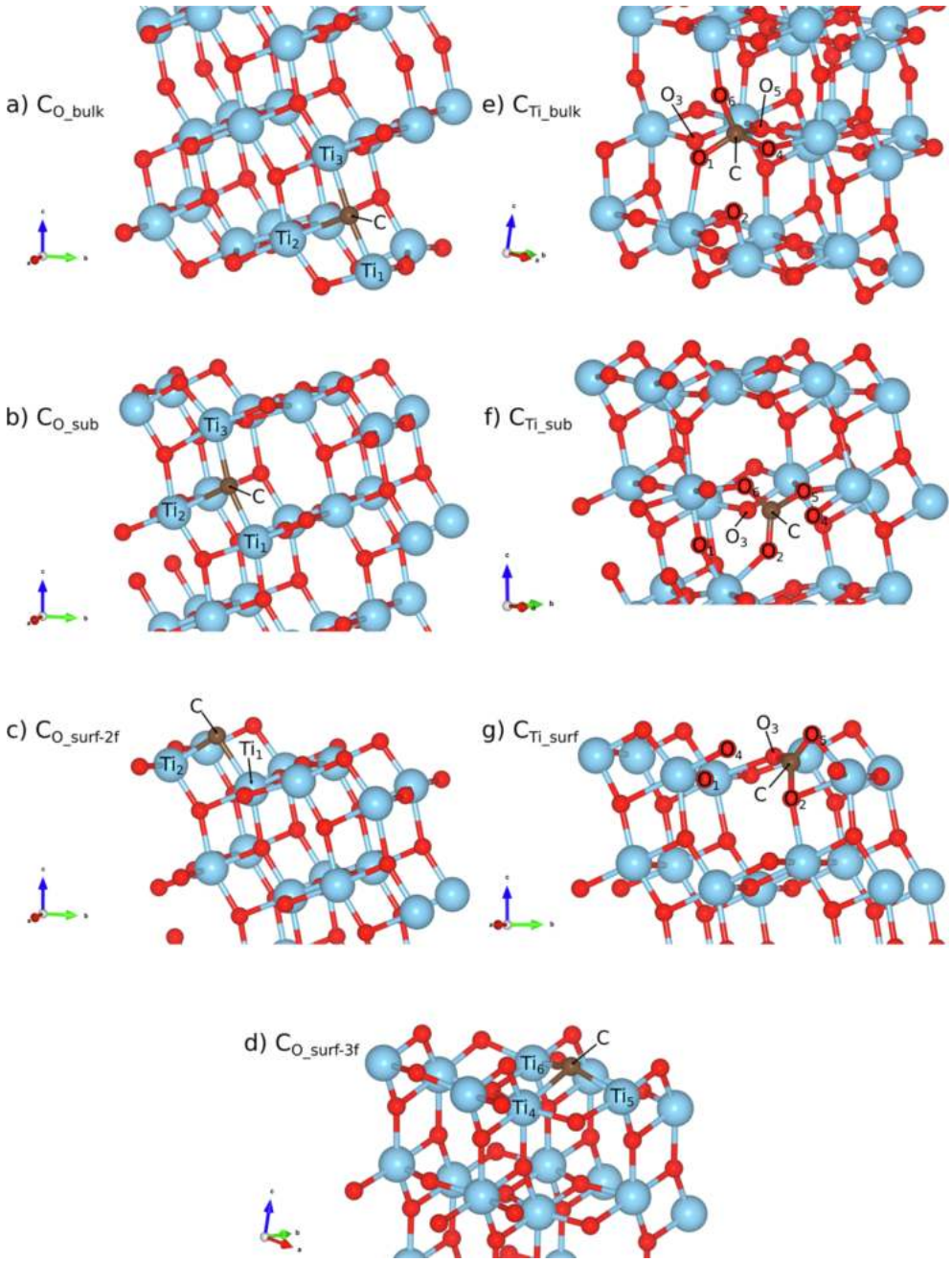

Fig. 3. Side view of the structure configurations following geometry relaxation with carbon doping on a-TiO_2 (1 0 1) surface. The blue, red, and brown spheres represent titanium, oxygen, and carbon, respectively. (For interpretation of the references to colour in this figure legend, the reader is referred to the web version of this article.)

defects calculations, the bottom two layers were kept frozen at the optimized bulk positions, whereas the top two layers were allowed to relax. All layers were allowed to relax for bulk defect calculations.

3. Results and discussion

3.1. Structure and bonding analyses

Geometry relaxation for C-doped a-TiO_2 (1 0 1) is illustrated in Fig. 3 with the bond lengths tabulated in Table 1. For the C_O defects, the majority of the C_O-Ti bonds lengthen more than the O—Ti bonds of pristine a-TiO_2 (1 0 1). This result is most likely because the carbon electronegativity is smaller than that of oxygen; one may also expect that the electronegativity difference between carbon and oxygen will affect the charge distributions and optical response, which will be discussed later. Notably, the C_O-Ti_1 bond on $C_{O\_surf-2f}$ sites confers a 13.9% decrease in bond length, a finding consistent with previous theoretical studies of C–doping on TiO_2 [20,37].

For C_{Ti} defects, the geometric distortions are large, as the Ti and C atoms have different coordination numbers. The influence of C_{Ti} significantly alters the neighboring O-bonding of the Ti atom by not keeping previous configuration from six-coordinates in pristine a-TiO_2 (1 0 1) to four-coordinates for C_{Ti_bulk} (Fig. 3e) and three-coordinate for C_{Ti_sub} (Fig. 3f) and $C_{Ti\ surf}$ (Fig. 3g). To compensate for the C_{Ti_bulk} atom's bonding with the O atoms, two of the C—O bonds (C_{Ti}—O_4 and C_{Ti}—O_6) shrink almost equally, implying the presence of some degree of covalent response, while the remaining two C–O bonds (C_{Ti}-O_1 and C_{Ti}-O_5) expand sufficiently to form the corresponding four-coordinate

Table 1
Optimized bond lengths (in Å) for select C-doped a-TiO_2 (1 0 1). Values parentheses are bond lengths for the undoped, pristine a-TiO_2 (1 0 1).

Bond	C_{O_bulk}	C_{O_sub}	$C_{O\_surf\text{-}2f}$	$C_{O\_surf\text{-}3f}$
C_O-Ti_1	1.951 (1.788)	2.073 (1.888)	1.832 (2.128)	–
C_O -Ti_2	2.231 (2.037)	2.195 (1.956)	1.961 (1.837)	–
C_O -Ti_3	2.075 (1.985)	2.105 (2.077)	–	–
C_O -Ti_4	–	–	–	2.318 (2.038)
C_O -Ti_5	–	–	–	2.078 (1.964)
C_O -Ti_6	–	–	–	2.078 (1.964)
Bond	C_{Ti_bulk}	C_{Ti_sub}	C_{Ti_surf}	–
C_{Ti}-O_1	1.407 (1.954)	2.860 (1.975)	2.189 (1.999)	–
C_{Ti}-O_2	2.737 (1.985)	1.365 (2.000)	1.312 (1.786)	–
C_{Ti}-O_3	2.696 (1.938)	2.129 (1.937)	1.280 (1.964)	–
C_{Ti}-O_4	1.360 (1.938)	2.118 (1.937)	3.033 (1.963)	–
C_{Ti}-O_5	1.506 (1.997)	1.365 (1.992)	1.287 (1.837)	–
C_{Ti}-O_6	1.383 (1.852)	1.285 (1.888)	–	–

configuration. C_{Ti_sub} and $C_{Ti\ surf}$, on the other hand, have one of the C-O bonds enlarge to form the respective three-coordinated configuration, consistent with previous reports [20]. The C doping on the C_{Ti} defect site creates one unpaired electron on the C sites and two unpaired electrons on the nonbonding O sites. The C doping on C_{Ti} defect site causes one unpaired electron on the C sites and two unpaired electrons on the non-bonding O site.

To investigate the nature of the chemical bonding further, overlap population (OP) analyses of the major atoms involved in the C doping in the bulk, subsurface, and surface regions for a-TiO_2 (1 0 1) were undertaken. Table 3 displays the OP values for the selected bonding neighborhood with C dopants. The OP of pristine a-TiO_2 (1 0 1) is presented in parentheses; notably, the OP values differ for the various bonding sites, indicating that the OP is affected differently by different levels of bonding sites [38]. The OP for C_O models indicates an increase in C_O-Ti_3 bonding in C_{O_bulk} and C_{O_sub} sites, and C_O—Ti_2 bonding in $C_{O\_surf\text{-}2f}$ sites due to charge migration after the incorporation of C atom [39]. On the other hand, for C_{Ti} defect models, four C_{Ti}—O bonds are formed surrounding C atom in C_{Ti_bulk} site, and three C_{Ti}—O bonds are formed surrounding C atom in C_{Ti_sub} and C_{Ti_surf} sites. The OP values for all C_{Ti}—O bonds increase with a bigger effect observed on C_{Ti_bulk} and C_{Ti_surf}, inferring the short interatomic distances of the C-O bond lengths [40]. Further, C_{Ti}—O bonds on the C_{Ti_surf} site appear to be stronger with values greater than unity when compared to C_{Ti_bulk}, due to fewer atoms to bond and leading to a stronger atomic interaction.

The charge density distributions of the pristine and C-doped a-TiO_2 (1 0 1) systems (Fig. 4) are visualized to support the OP analyses. The

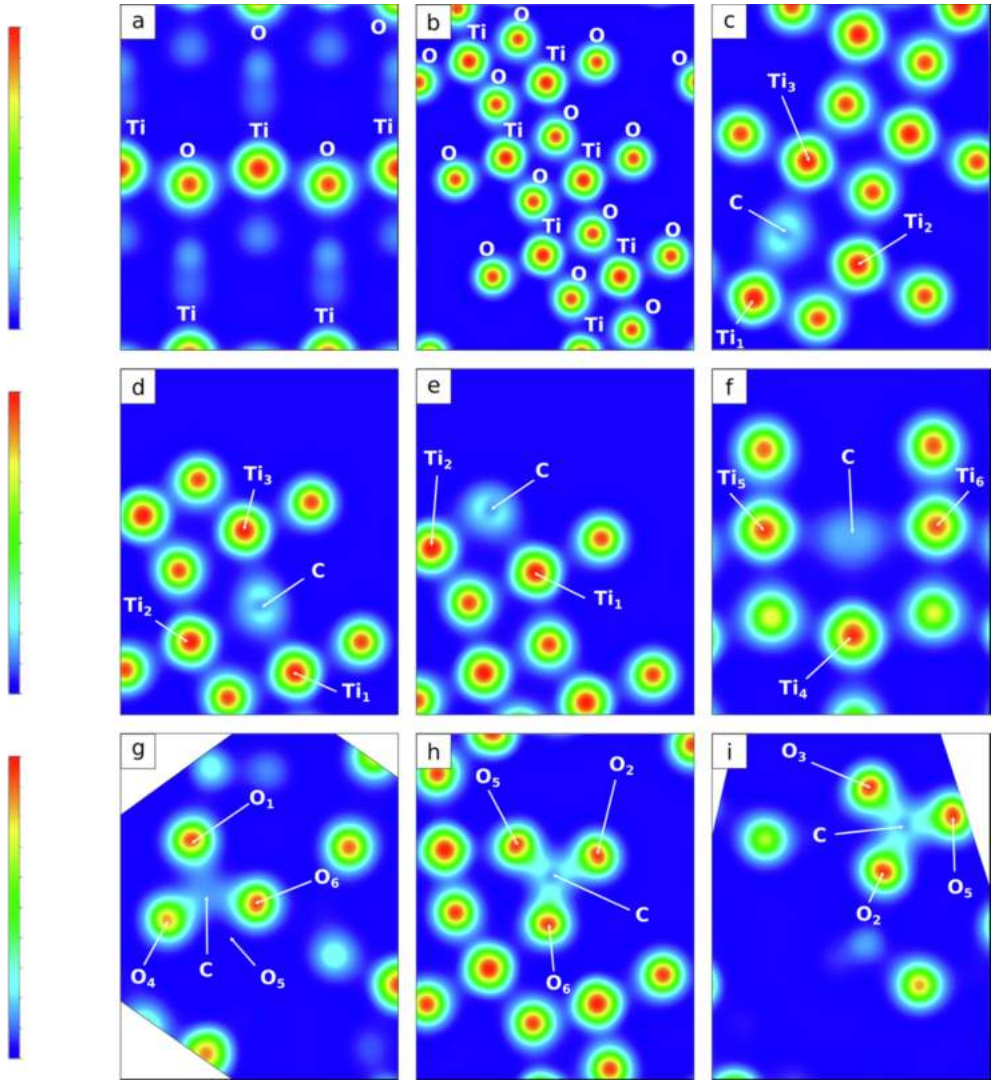

Fig. 4. Charge densities for (a) pristine a-TiO_2 viewed along (0 0 1), (b) pristine a-TiO_2 viewed along (1 0 0), (c) C_{O_bulk}, (d) C_{O_sub}, (e) $C_{O\_surf\text{-}2f}$, (f) $C_{O\_surf\text{-}3f}$, (g) C_{Ti_bulk}, (h) C_{Ti_sub}, and (i) C_{Ti_surf} are represented from blue (0.00 eÅ^{-3}) to red (1.26 eÅ^{-3}). (For interpretation of the references to colour in this figure legend, the reader is referred to the web version of this article.)

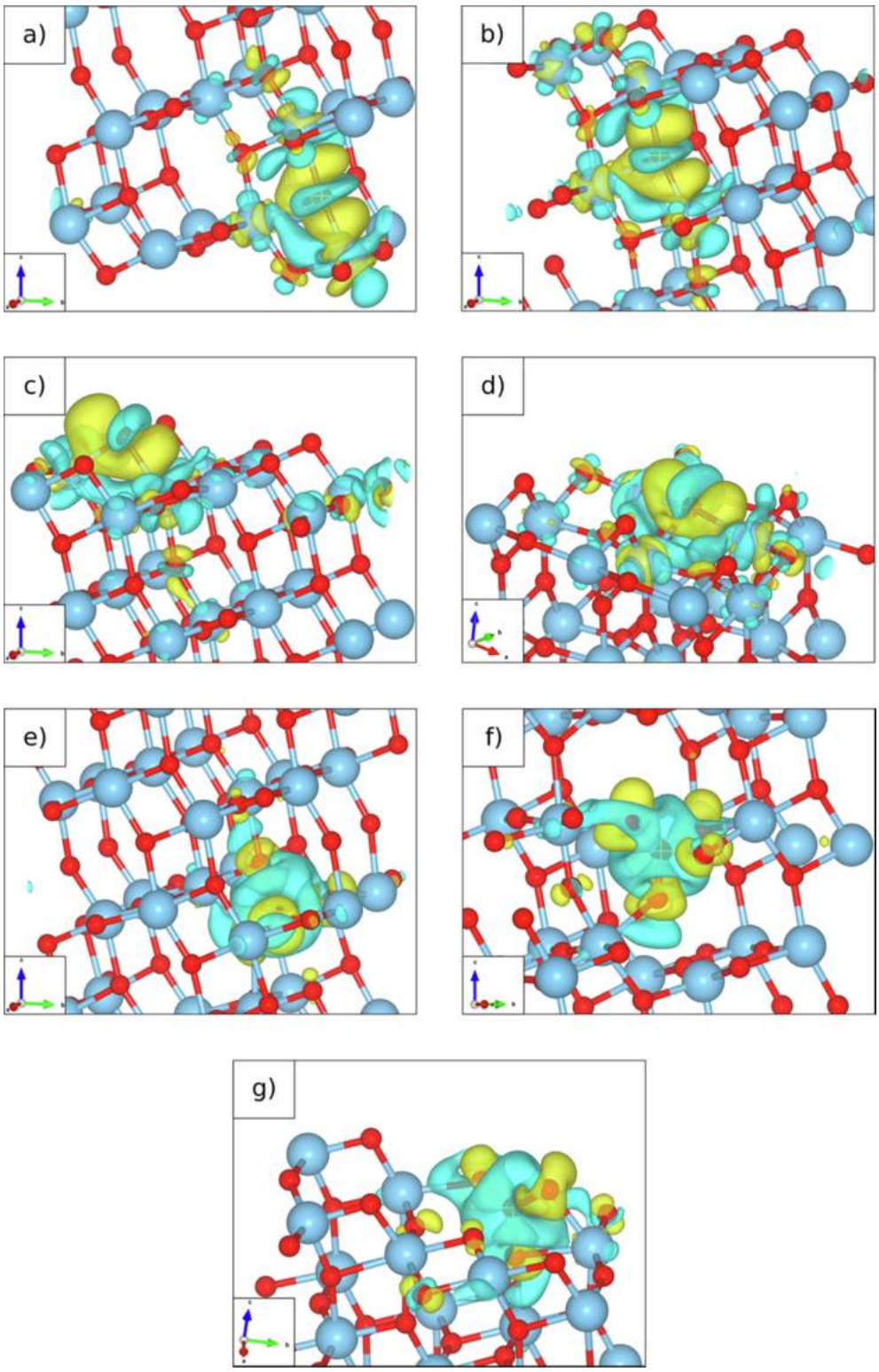

Fig. 5. The charge density difference plot for C-doped a-TiO_2 catalytic system at multi- sites level. (a) C_{O_bulk}, (b) C_{O_sub}, (c) $C_{O\_surf\text{-}2f}$, (d) $C_{O\_surf\text{-}3f}$, (e) C_{Ti_bulk}, (f) C_{Ti_sub}, and (g) C_{Ti_surf}.

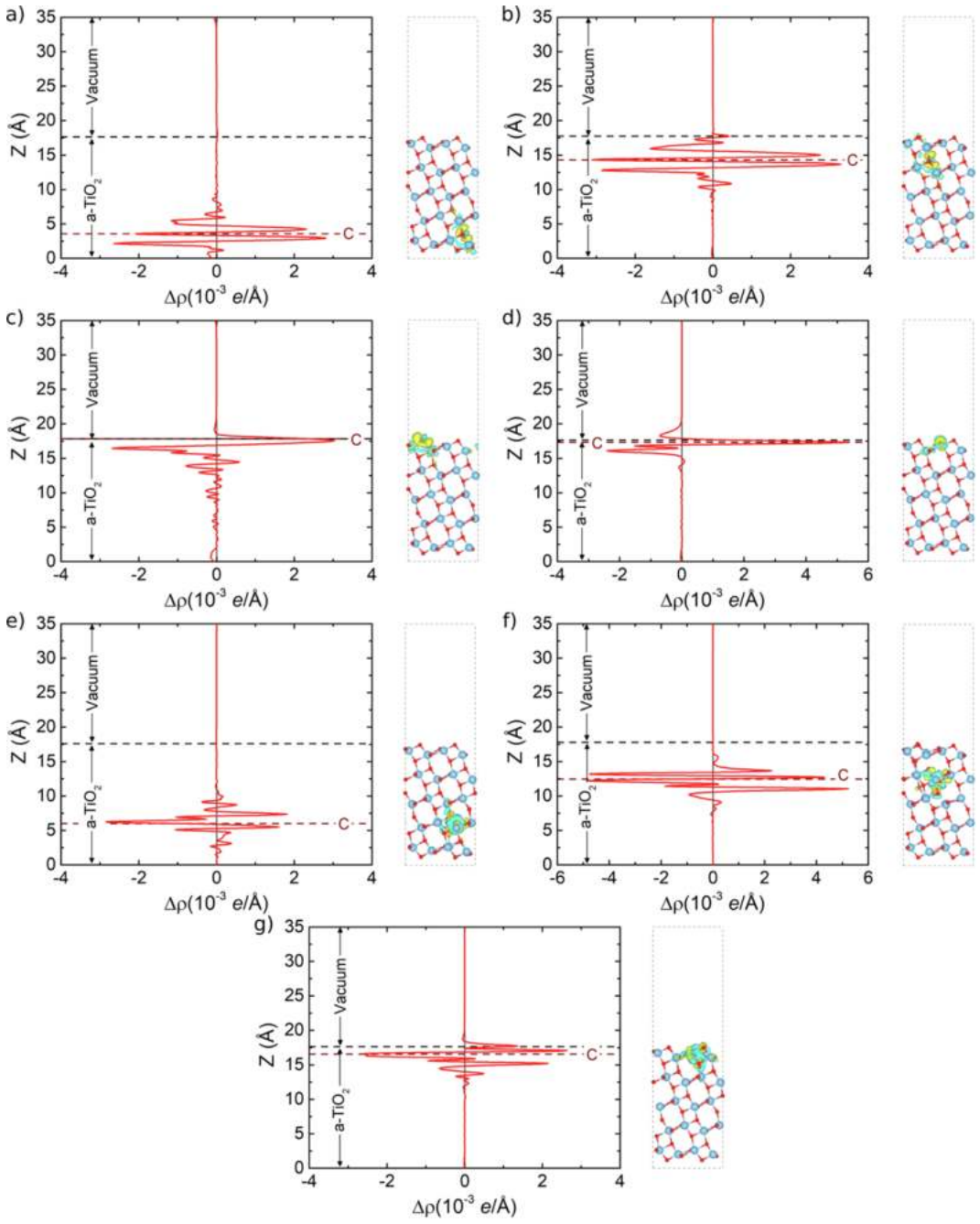

Fig. 6. Planar averaged charged density differences, $\Delta\rho$, along the Z direction (graph) and charge density difference with an isosurface (image) for (a) C_{O_bulk}, (b) C_{O_sub}, (c) $C_{O\_surf\text{-}2f}$, (d) $C_{O\_surf\text{-}3f}$, (e) C_{Ti_bulk}, (f) C_{Ti_sub}, and (g) C_{Ti_surf}.

charge distributions of the Ti and O atoms in the pristine a-TiO_2 (Fig. 4 (a–b)) and all C_O defect models (Fig. 4 (c–f)) are similar, with the charge density around the C atom in the C_O defect models being spherical, indicating that there is no covalent bonding with neighbouring Ti; this result suggests that the C atoms act primarily in an ionic type interaction with the surrounding Ti cations. On the other hand, the charge densities in the C_{Ti} defect models (Fig. 4 (g–i)) reveal that the C atoms form covalent bonds with neighboring O atoms. Fig. 4 (g) exhibits three major covalent interactions (C_{Ti}-O_1, C_{Ti}-O_4, and C_{Ti}-O_6); there is also a covalent interaction (C_{Ti}-O_5) on C_{Ti_bulk} site defect. Meanwhile, Fig. 4 (h) and 4 (i) reveal the three covalent interactions on C_{Ti_sub} (C_{Ti}-O_2, C_{Ti}-O_5,and C_{Ti}-O_6) and C_{Ti_surf} (C_{Ti}-O_2, C_{Ti}-O_3, and C_{Ti}-O_5), respectively. Consequently, the charge distributions in Fig. 4 concur well with the results of previous OP analysis [41].

Atomic net charges for pristine and C–doped a-TiO_2 (1 0 1) were determined using Bader analysis for the C dopant and surrounding

Table 2
Overlap population (in a.u) values for a specified bond in pristine (in parentheses) and C–doped a-TiO_2 101 slab models.

Bond	C_{O_bulk}	C_{O_sub}	$C_{O\_surf\text{-}2f}$	$C_{O\_surf\text{-}3f}$
C_O-Ti_1	0.522 (0.650)	0.751 (0.948)	0.492 (0.597)	–
C_O -Ti_2	0.281 (0.348)	0.405 (0.574)	1.032 (0.756)	–
C_O -Ti_3	0.399 (0.318)	0.398 (0.349)	–	–
C_O -Ti_4	–	–	–	0.316 (0.353)
C_O -Ti_5	–	–	–	0.506 (0.532)
C_O -Ti_6	–	–	–	0.518 (0.561)
Bond	C_{Ti_bulk}	C_{Ti_sub}	C_{Ti_surf}	
C_{Ti}-O_1	0.938 (0.378)	0.020 (0.562)	0.114 (0.601)	–
C_{Ti}-O_2	0.048 (0.318)	0.860 (0.569)	1.330 (0.801)	–
C_{Ti}-O_3	0.073 (0.319)	0.160 (0.506)	1.582 (0.562)	–
C_{Ti}-O_4	0.955 (0.320)	0.163 (0.507)	0.136 (0.561)	–
C_{Ti}-O_5	0.727 (0.339)	0.741 (0.640)	1.612 (1.173)	–
C_{Ti}-O_6	0.923 (0.407)	0.946 (0.948)	–	–

Table 3
Net charges (in *e*) for selected atoms in pristine (in parentheses) and C–doped a-TiO2 101 slab models.

Atom	C_{O_bulk}	C_{O_sub}	$C_{O\_surf\text{-}2f}$	$C_{O\_surf\text{-}3f}$
C_O	−0.80 (-1.13)	−0.87 (-1.18)	−0.64 (-1.01)	−0.89 (-1.22)
Ti_1	+2.20 (+2.33)	+2.31 (+2.33)	+2.24 (+2.32)	–
Ti_2	+2.30 (+2.32)	+2.29 (+2.41)	+1.91 (+2.29)	–
Ti_3	+2.24 (+2.38)	+2.23 (+2.32)	–	–
Ti_4	–	–	–	+2.31 (+2.32)
Ti_5	–	–	–	+2.12 (+2.21)
Ti_6	–	–	–	+2.12 (+2.21)
Atom	C_{Ti_bulk}	C_{Ti_sub}	C_{Ti_surf}	
C_{Ti}	+1.39 (+2.38)	+1.68 (+2.32)	+1.83 (+2.21)	–
O_1	−0.87 (-1.18)	−1.01 (-1.18)	−1.06 (-1.19)	–
O_2	−0.98 (-1.13)	−1.01 (-1.18)	−1.04 (-1.10)	–
O_3	−1.00 (-1.21)	−1.09 (-1.21)	−1.11 (-1.22)	–
O_4	−0.98 (-1.21)	−1.09(-1.21)	−1.02 (-1.22)	–
O_5	−0.92 (-1.22)	−0.97 (-1.19)	−1.02 (-1.02)	–
O_6	−0.97 (-1.17)	−0.97 (-1.17)	–	–

Table 4
Formation energies of C-doped defect at different level sites of a-TiO_2 (1 0 1). The most stable defect site for each environment is indicated in bold.

Doped system	Formation energy (eV)	
	O-rich	Ti-rich
C_{O_Bulk}	13.61	1.07
C_{O_Sub}	13.73	1.19
$C_{O\_Surf\text{-}2f}$	13.68	1.14
$C_{O\_Surf\text{-}3f}$	13.81	1.27
C_{Ti_Bulk}	19.2	9.14
C_{Ti_Sub}	14.10	4.04
C_{Ti_Surf}	**10.8**	**0.74**

atoms, Table 4. The atomic net charge is labelled using the atom arrangement based in Fig. 1. C doping results in small variations on the atomic net charge in the C_O defect model, with the net charge for Ti surrounded by Co rise of less than 20% (from + 1.9 to + 2.3). The sign of the C atom charged is reversed from positive to negative, reflecting the anion behaviour when substituting an O atom. Further, Ti atoms that surround the dopant donate electron density, as the net charge value decreases by about 2% on average across all cases.

Charge density differences are presented in Fig. 5. The charge depletion and accumulation regions are more prominent around C dopant sites, consistent with the Bader charge analyses. In comparison to the C_O defect, which has a larger charge distribution on the C dopant as shown in Fig. 5 (a-d), the C_{Ti} system has a narrower charge distribution on the C dopant. The results in Fig. 5 (e-g) attest to the increment in the bond strengths of C-Ti and C-O. For surfaces, the higher degree of charge transfer and larger charge density accumulation on the top of the surface, as shown in Fig. 5 (c) and (d) for C_O model, will result in the formation of a strong, built-in surface electric fields. The C_{Ti} defect, Fig. 5 (g), has the lowest charge transfer and low charge density. Meanwhile, the planar-averaged electron density difference along the Z-direction revealed changes of charge density (Fig. 6), where charge depletion and charge accumulation are represented by negative and positive values, respectively.

3.2. Defect formation energy

To estimate impurity stability, defect formation energies (E_{form}) were determined using the equation (1) [42]:

$$E_{form} = E(defect) - E(defect\_free) + \sum_{\alpha} n_{\alpha}\mu_{\alpha} \quad (1)$$

where E(defect) is the total energy of C-doped a-TiO_2 (1 0 1) slab, E (defect_free) is the total energy of a-TiO_2 (1 0 1) slab without defects, μ_α is the reference chemical potential of the elemental species (α = C, Ti, O) with the number of atoms (n_α) transferred from the defect free system. The stability of various configurations is dependent on the chemical potential of oxygen (μ_O) and the growth conditions. The chemical potential of a-TiO_2 is satisfied by equation (2),

$$\Delta H_{form}(TiO_2) = \mu_{Ti} + 2\mu_O \quad (2)$$

which has been calculated to be $\Delta H_{form}(TiO_2) = -9.73eV$. The system is in equilibrium with oxygen gas under O-rich conditions, resulting in a $\mu_O = 0$, thus, $\mu_{Ti} = -9.73eV$ is obtained. Under limiting O-poor (Ti-rich) conditions, TiO_2 energy formation is in thermodynamic equilibrium with Ti_2O_3[42], in which the chemical potential is described by equation (3):

$$\Delta H_{form}(Ti_2O_3) = 2\mu_{Ti} + 3\mu_O \quad (3)$$

which has been calculated to be $\Delta H_{form}(Ti_2O_3) = -15.39eV$. By comparing equations (2) and (3), $\mu_O = -4.07eV$ and $\mu_{Ti} = -1.59eV$ are obtained. The chemical potential of carbon, μ_C (−1.26 eV) is calculated using bulk carbon.

The formation energies were determined for the two O-rich and Ti-rich conditions, with pertinent results presented in Table 2. The formation energies for the C_O sites suggests that substitution in the bulk is more favorable than substitution at other sites for both O-rich and Ti-rich conditions, followed by $C_{O\_Surf\text{-}2f}$ with energy difference of only 0.07 eV. From Table 2, it is observed that C_O sites may be easier to substitute in a Ti–rich condition than in an O–rich environment. The preferred order for C_O energy formation is $C_{O\_Bulk} > C_{O\_Surf\text{-}2f} > C_{O\_Sub} > C_{O\_Surf\text{-}3f}$. For C-doped a-$TiO_2$ (1 0 1) at Ti sites, however, the formation energy is more favorable on the surface than at other sites for both O-rich and Ti-rich conditions. The preferred order for C_{Ti} energy formation is $C_{Ti\_Surf} > C_{Ti\_Sub} > C_{Ti\_Bulk}$. In general, C dopants prefer to replace Ti atoms at the surface, but since the difference in formation energy at Co for all level sites is small, C dopant could replace any oxygen atoms at any level site in the case of high doping concentration.

3.3. Electronic structure

Spin-polarized total and projected densities of states (TDOS and PDOS, respectively) for pristine and C-doped a-TiO_2 (1 0 1) are illustrated in Fig. 7, while Fig. 8 shows the spin polarized band structures

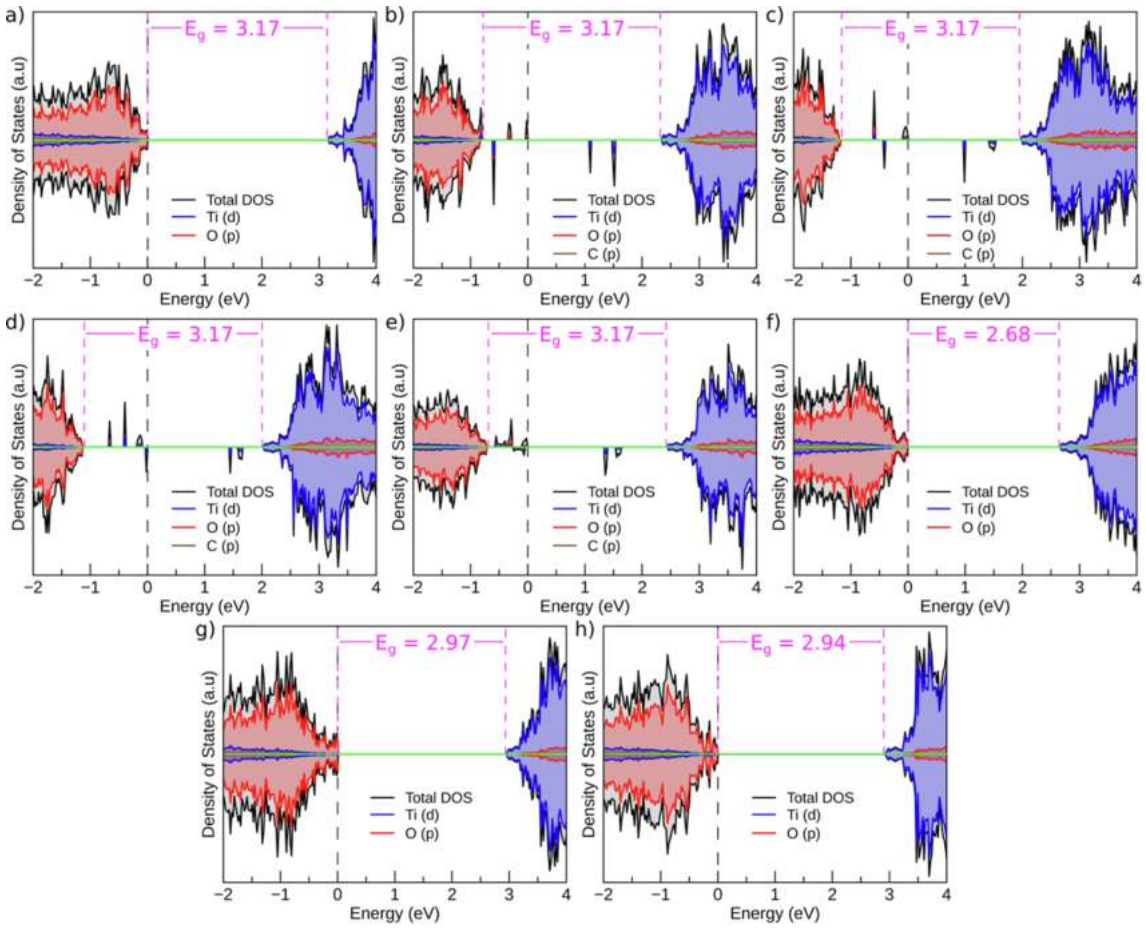

Fig. 7. Total and projected density of states for C–doped a-TiO_2 (1 0 1) systems for (a) pristine a-TiO_2 (b) C_{O_bulk}, (c) C_{O_sub}, (d) $C_{O\_surf\text{-}2f}$, (e) $C_{O\_surf\text{-}3f}$, (f) C_{Ti_bulk}, (g) C_{Ti_sub}, and (h) C_{Ti_surf}. The vertical black dashed lines and solid green lines denote the Fermi level and zero DOS, respectively. Magenta dashed lines indicate the various gap boundaries. (For interpretation of the references to colour in this figure legend, the reader is referred to the web version of this article.)

along high symmetry lines within the first Brillouin zone. For pristine a-TiO_2 (1 0 1), the DOS indicate that the valence band is dominated by O *2p* electron states, whereas the conduction band is dominated by Ti *3d* electron states. The DOS have a symmetrical x–axis shape. The band structure (Fig. 8 (a)) has identical spin-up and spin-down states, indicating that their net magnetic moment is zero. There are no impurity states observed between the valence and conduction bands, as shown in Fig. 7 (a) and Fig. 8 (a). The calculated band gap of 3.17 eV is 3% larger than the experimental value of *ca*. 3.20 eV [33,34]. According to the band structure diagram in Fig. 8 (a), the absorption transition is consistent with an indirect semiconductor with identical spin-up and spin-down band structures for pristine a-TiO_2 (1 0 1), consistent with previous experimental and theoretical reports [18,43,44].

In the case of C_O defects, the conduction band is dominated by Ti 3*d* states and the valence band is dominated by O *2p* states for bulk, subsurface, surface-2f and surface-3f. Fig. 7 (b–e) and Fig. 8 (b–e) show impurity states observed between the valence and conduction bands. Surprisingly, there is no variation in band gap when compared to pristine a-TiO_2 (1 0 1), with only the position of the Fermi level affected. The DOS for C atoms are exclusively in the band gap region, which induces the formation of Ti and O states in the forbidden gap. Further, unoccupied spin-down impurity states are visible below the CBM at energies ranging from 0.36 to 1.06 eV, with $C_{O\_Surf\text{-}2f}$ having the smallest gap. As a result, excited electrons returning from CBM to VBM may be trapped by unoccupied defect states and undergo recombination with holes at VBM. This will result in a red shift absorption at the band edge. It can be deduced from Fig. 8 (b–e) that the C_O defect exhibits indirect semiconductor behavior.

Fig. 7 (f–h) reveals that for C_{Ti} model defects that the conduction band is dominated by Ti *3d* states and the valence band by O *2p* states for the bulk, subsurface, and surface models. Meanwhile, as shown in Fig. 7 (f–h) and Fig. 8 (f–h), no impurity states are observed between the valence and conduction bands. The host band gap decreases from 3.17 eV to 2.68 eV, 2.97 eV, and 2.94 eV for bulk, subsurface, and surface, respectively, with the Fermi level close to the valence band. As the band gap narrows, it is expected that the absorption will shift from the UV to blue region. This result is most likely due to the large distortion caused by the C atom when a Ti atom is replaced. Further, the DOS of C atoms are observed in neither the valence band, conduction band, nor band gap, indicating that the existence of C does not greatly affect the

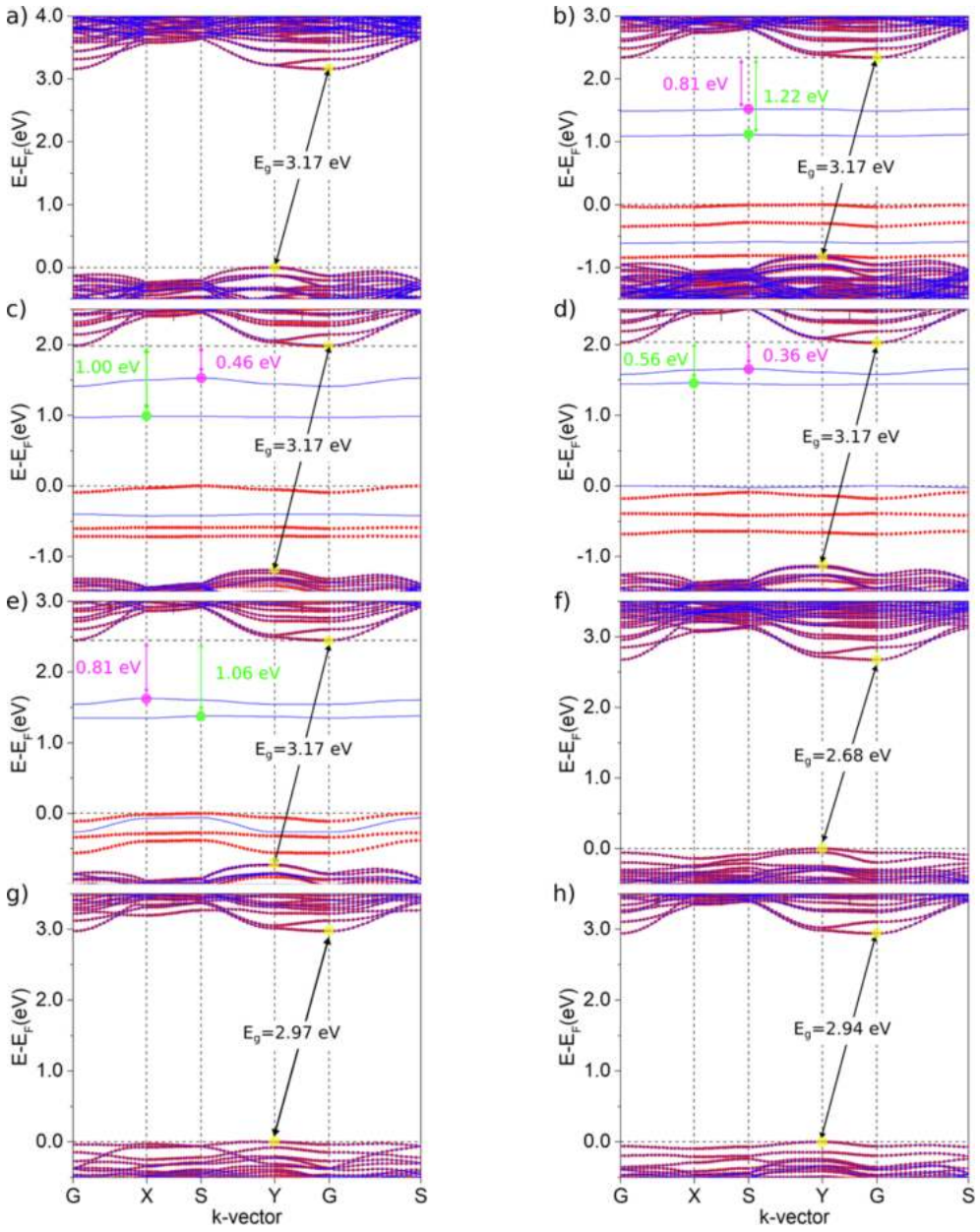

Fig. 8. Band structures for pure and C-doped a-TiO_2 (1 0 1) system for (a) pristine a-TiO_2 (b) C_{O_bulk}, (c) C_{O_sub}, (d) $C_{O\_surf\text{-}2f}$, (e) $C_{O\_surf\text{-}3f}$, (f) C_{Ti_bulk}, (g) C_{Ti_sub}, and (h) C_{Ti_surf}.

electronic properties. It can be deduced from Fig. 8 (f–h) that the C_{Ti} defect exhibits indirect semiconductor behaviour.

3.4. Absorption spectra

Optical properties were determined using the Kramer–Kronig transformation [45,46]. The dielectric function, $\varepsilon_{ij}(\omega)$ is derived by sum of the refractive index n and the extinction coefficient k (equation (4)):

$$\varepsilon_{ij}(\omega) = n_{ij}(\omega) + ik_{ij}(\omega) \quad (4)$$

By taking the imaginary part of the dielectric function, the absorption spectra can be obtained. Although this method has several limitations due to its neglect of excitation factors [47], such as electron–hole interaction and excitonic effects, it is utilised here to provide a preliminary description of the relative visual properties of pristine and C–doped a-TiO_2 (1 0 1) materials.

Calculated absorption spectra for C-doped a-TiO_2 (1 0 1) are presented in Fig. 9., which demonstrate how the substitution of a C dopant can significantly alter the optical characteristics of a-TiO_2. Unfortunately, there are some notable limitations of the adopted methodology

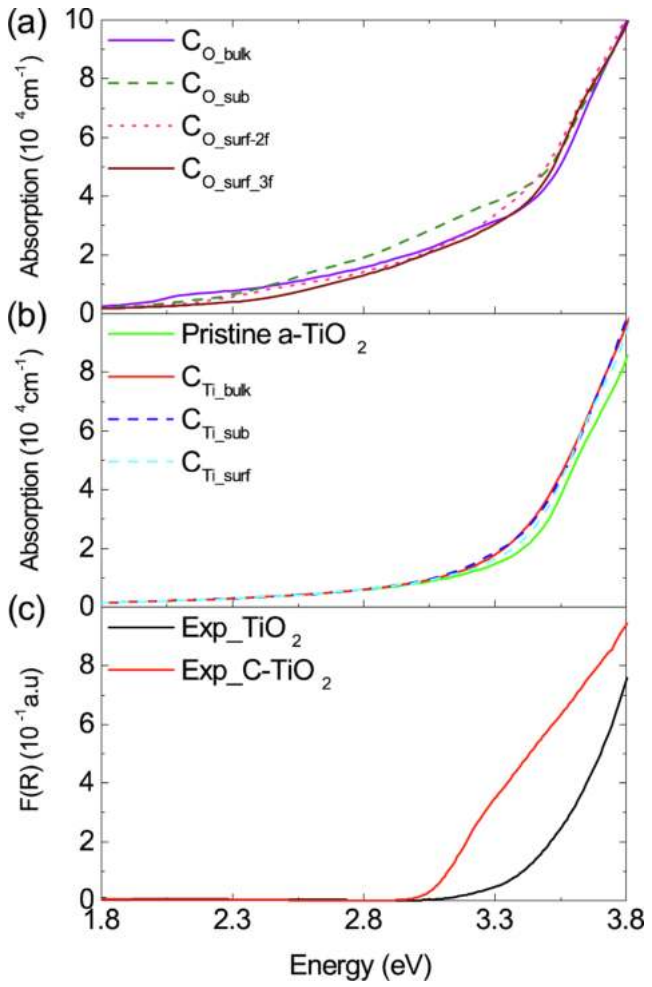

Fig. 9. Optical absorption of simulated spectra of (a) C_O, (b) pristine and C_{Ti}, as well as experimental spectra of (c) pristine and C-doped spectra TiO_2 (1 0 1).

and the choice of U parameter, which is based on balancing of optical and structural optimization as previously discussed, that limits complete agreement. In particular, the Hubbard term and the electron or hole traps will have an effect on the absorption spectra pattern [32,47], resulting significant red-shift with curve appears to fit each other reasonably and result in an increase in absorbance in the visible area. C_O defects confer an increase in absorbance in the visible and UV spectrums [48], with the majority of the spectrum covered on C_{O_sub}, consistent with DOS and band structure analysis. In particular, each small peak can be assigned to a specific impurity state transition generated by the C dopant distinguishable from others. The absorption region is red shifted for C_{Ti} defects due to the decrease in the electronic band gap. The predicted results concur with experimentally C-doped a-TiO_2 [49], which showed how the incorporation of C dopant into the a-TiO_2 host could reduce its electronic band gap and improve its absorption performance.

3.5. Photocatalytic applications

Based on the DFT calculation of C-doped TiO_2 (1 0 1), the band gap of the C-doped TiO_2 (1 0 1) and photocatalytic mechanism application under UV and visible light irradiation has been determined. The lowest formation energy of C-doped TiO_2 (1 0 1) is at C_{Ti_surf} with band gap 2.94 eV. In Fig. 10 (a), a schematic diagram of photocatalytic oxidation over C-doped TiO_2 has been proposed. C-doping of the Ti atom at the surface between the carbon part and TiO_2 could cause distortion of the composite lattice structure. Subsequently, carbon defects were introduced between the conduction and valence bands of TiO_2, and electrons can be promoted to the conduction band from the impurity level with ease, narrowing the band gap (2.94 eV) and making the composite lattice structure more stable. The DFT-determined potentials of the CB and VB for the C-doped TiO_2 (1 0 1) are 0.00 and + 2.94 eV (vs. NHE), respectively. In this case, the possible reaction that could occur is oxidation since the reaction is preferred to occur at positive value of NHE, which is more likely to valence band. This result is in agreement with a prior study that focused on photocatalytic degradation of methyl ethyl ketone over carbon-doped TiO_2 film under visible light irradiation [50]. The calculated CB and VB for the C-doped TiO_2 was −1.90 and + 2.48 eV, respectively, which agrees with our study. The NHE value that was reported can be correlated to the behaviour for oxidation process in photocatalytic reaction [50]. Reported by Nath et al., selective photocatalytic oxidation of benzyl alcohol to benzaldehyde over carbon-doped TiO_2 can occur at 2.51 eV under UV/Vis light irradiation [51]. However, no further explanation was provided regarding the NHE redox potential calculation. From the results presented here, we hypothesize that this position of carbon doping is more suitable for the application of photocatalytic oxidation reaction due to the band gap that is appropriated for oxidation process of volatile organic compound.

It is also possible to utilize the C-doped TiO_2 material for the photocatalytic reduction of CO_2, as illustrated in Fig. 10 (b). The most appropriate band gap that could be used is 3.17 eV represented by C_{O_bulk}. The calculated potential of CB and VB for C_{O_bulk} are 0.73 and + 2.44 eV, respectively. This indicates that the CB value of C_{O_bulk} is nearest to the alignment of CB value for CO_2 reduction redox potential, inferring electron transportation could be achieved. Our previous work has shown that CO_2 could be converted into methanol with high yield under UV/Vis light irradiation over C-doped TiO_2 with 3.10 eV band gap [49]. According to the mechanism that has been proposed in Fig. 10 (b), the band gap is attributed to the presence of C_{O_bulk}. Thus, we can deduce that certain band gap of C-doped TiO_2 could be exploited for specific photocatalytic reactions.

4. Conclusions

The surface, subsurface, and bulk C-doping of multi-layer a-TiO_2 (1 0 1) were evaluated with DFT to explore the geometric structure, chemical bonding, electronic structure, and optical properties of C-doped. The formation energy of C_{Ti_surf} is the lowest and most favourable among other doping sites. It also presents a significant distortion in the geometric structure surrounding the C dopant. The C atom could also potentially replace the O atom side due to the low formation energy. Moreover, there is no impurity in the band gap for all C_{Ti} models indicating a strong atomic interaction due to the bonding of fewer atoms , which confers to the red-shifted absorption. Meanwhile, for all C_O models, the defects lead to the introduction of impurity in the band gap consequently inducing absorption at visible and IR region. The

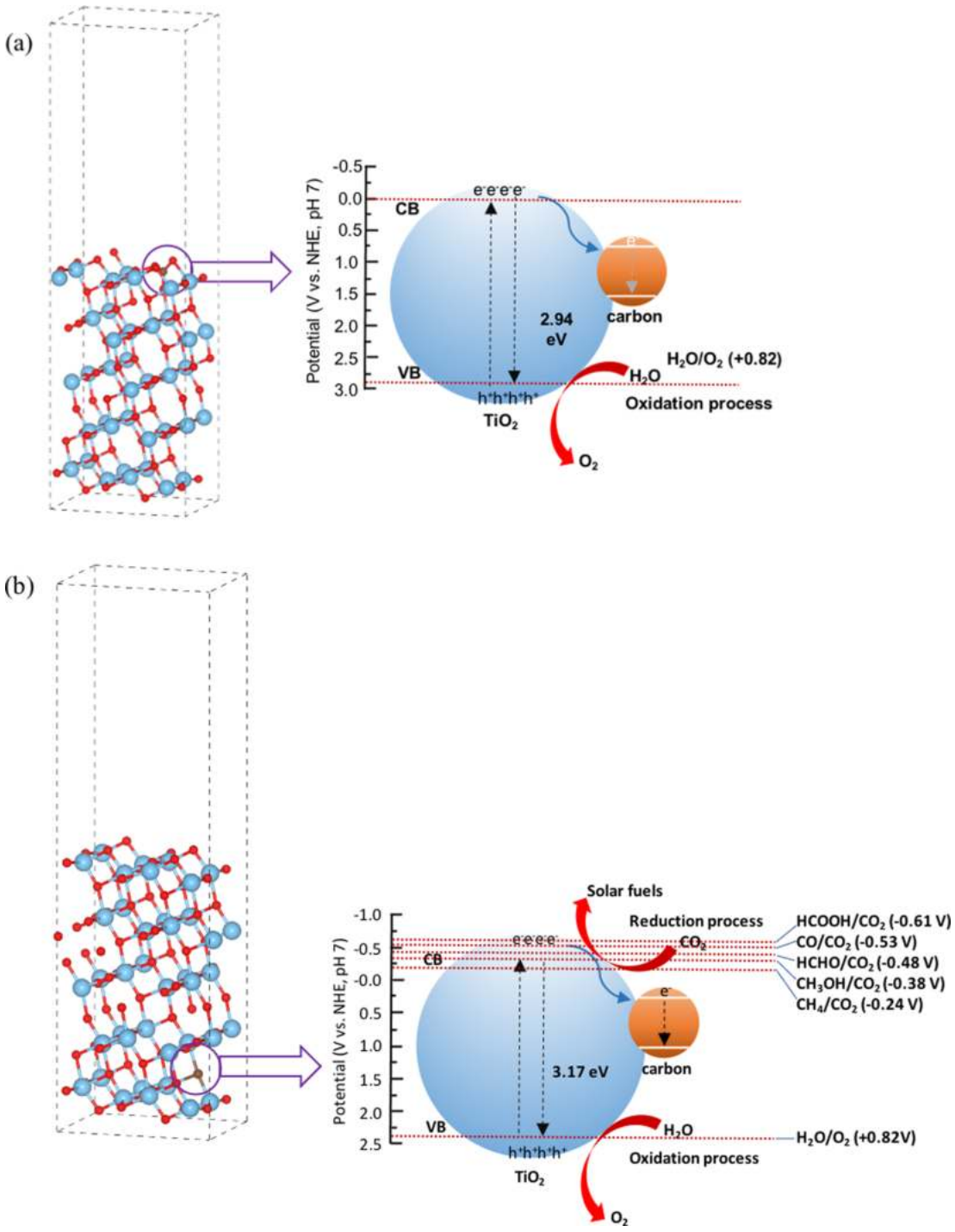

Fig. 10. Schematic diagram of mechanism for application of C-doped a-TiO_2 in (a) photocatalytic oxidation process and (b) photocatalytic reduction process.

calculated DFT absorption properties agree well with the experimental absorption spectra. The optimized carbon doping positions at C_{Ti_surf} and C_{O_bulk} in this study are suitable to be utilized in photocatalytic redox reaction. The present study provides insights for designing alternative thickness layers of C-doped a-TiO_2 (1 0 1) to obtain higher performance in photocatalytic applications.

CRediT authorship contribution statement

Nur Umisyuhada Mohd Nor: Conceptualization, Writing, Investigation. **Elham Mazalan:** Simulated and Interpreted theoretical DFT calculation. **Chad Risko:** Resources, Review & Revised. **Mark Crocker:** Resources. **Nor Aishah Saidina Amin:** Supervised, Edited, Visualized & Revised the manuscript.

Declaration of Competing Interest

The authors declare that they have no known competing financial interests or personal relationships that could have appeared to influence the work reported in this paper.

Acknowledgements

The authors would like to express their sincere gratitude to the Ministry of Higher Education (MOHE) Malaysia for the financial support received under the Fundamental Research Grant Scheme (FRGS), vot number 5F101) (FRGS/1/2018/TK02/UTM/01/2) and UTM Fundamental Research Grant (vot number 21H28). NUMN would like to thank MOHE for MyBrain15 Scholarship. EM would like to thank Universiti Teknologi Malaysia for UTM Fellowship Zamalah Scheme. NASA acknowledges the Fulbright fellowship programme by the Malaysian-American Commission On Educational Exchange (MACEE) for her visit to the University of Kentucky. CR acknowledges funding by the Research Corporation for Science Advancement (RCSA) Cottrell Scholars program (Award No. 24432). Computing resources on the Lipscomb High Performance Computing Cluster were provided by the University of Kentucky Information Technology Department and the Center for Computational Sciences (CCS).

Appendix A. Supplementary material

Supplementary data to this article can be found online at https://doi.org/10.1016/j.apsusc.2022.152641.

References:

[1] L. Kavan, M. Grätzel, S.E. Gilbert, C. Klemenz, H.J. Scheel, Electrochemical and Photoelectrochemical Investigation of Single-Crystal Anatase, J. Am. Chem. Soc. 118 (28) (1996) 6716–6723, https://doi.org/10.1021/ja9541721.

[2] Y. Liu, M. Wang, D. Li, F. Fang, W. Huang, Engineering self-doped surface defects of anatase TiO_2 nanosheets for enhanced photocatalytic efficiency, Appl. Surf. Sci. 540 (2021) 148330, https://doi.org/10.1016/j.apsusc.2020.148330.

[3] G. Li, K. Fang, Y. Ou, W. Yuan, H. Yang, Z. Zhang, Y. Wang, Surface study of the reconstructed anatase TiO_2 (001) surface, Prog. Nat. Sci. Mater. Int. 31 (2021) 1–13, https://doi.org/10.1016/j.pnsc.2020.11.002.

[4] W. Yuan, B. Zhu, K.e. Fang, X.-Y. Li, T.W. Hansen, Y. Ou, H. Yang, J.B. Wagner, Y. i. Gao, Y. Wang, Z.e. Zhang, In situ manipulation of the active Au-TiO 2 interface with atomic precision during CO oxidation, Science 371 (6528) (2021) 517–521.

[5] M. Wang, X. Zhang, R. Rao, N.X. Qian, Y.Q. Ma, Study on vapor-thermal synthesis and sulfur-doping of TiO_2/graphene composites, Appl. Surf. Sci. 507 (2020), 144856, https://doi.org/10.1016/j.apsusc.2019.144856.

[6] Y. Wang, Y.-X. Chen, T. Barakat, T.-M. Wang, A. Krief, Y.-J. Zeng, M. Laboureur, L. Fusaro, H.-G. Liao, B.-L. Su, Synergistic effects of carbon doping and coating of TiO_2 with exceptional photocurrent enhancement for high performance H_2 production from water splitting, J. Energy Chem. 56 (2021) 141–151, https://doi.org/10.1016/j.jechem.2020.08.002.

[7] N.U.M. Nor, E. Mazalan, N.A.S. Amin, Insights into enhancing photocatalytic reduction of CO_2: Substitutional defect strategy of modified g-C_3N_4 by experimental and theoretical calculation approaches, J. Alloys Compd. 871 (2021), 159464, https://doi.org/10.1016/j.jallcom.2021.159464.

[8] X. Han, L. An, Y. Hu, Y. Li, C. Hou, H. Wang, Q. Zhang, Ti_3C_2 MXene-derived carbon-doped TiO_2 coupled with g-C_3N_4 as the visible-light photocatalysts for photocatalytic H_2 generation, Appl. Catal. B Environ. 265 (2020), 118539, https://doi.org/10.1016/j.apcatb.2019.118539.

[9] M.D. Calisir, M. Gungor, A. Demir, A. Kilic, M.M. Khan, Nitrogen-doped TiO_2 fibers for visible-light-induced photocatalytic activities, Ceram. Int. 46 (2020) 16743–16753, https://doi.org/10.1016/j.ceramint.2020.03.250.

[10] Z. Noorimotlagh, I. Kazeminezhad, N. Jaafarzadeh, M. Ahmadi, Z. Ramezani, Improved performance of immobilized TiO_2 under visible light for the commercial surfactant degradation: Role of carbon doped TiO_2 and anatase/rutile ratio, Catal. Today. 348 (2020) 277–289, https://doi.org/10.1016/j.cattod.2019.08.051.

[11] Q. Wang, B. Rhimi, H. Wang, C. Wang, Efficient photocatalytic degradation of gaseous toluene over F-doped TiO_2/exfoliated bentonite, Appl. Surf. Sci. 530 (2020), 147286, https://doi.org/10.1016/j.apsusc.2020.147286.

[12] P. Richardson, M.L.N. Perdigoto, W. Wang, R.J.G. Lopes, Manganese and Copper Doped Titania Nanocomposites for the Photocatalytic Reduction of Carbon Dioxide into Methanol, Nano Energy. 126 (2012) 200–207.

[13] B. Akhtar, H. Ghafuri, A. Rashidizadeh, Synergistic effect of iodine doped TiO_2 nanoparticle/g-C_3N_4 nanosheets with upgraded visible-light-sensitive performance toward highly efficient and selective photocatalytic oxidation of aromatic alcohols under blue LED irradiation, Mol. Catal. 506 (2021), 111527, https://doi.org/10.1016/j.mcat.2021.111527.

[14] Q. Guo, L. Fu, T. Yan, W. Tian, D. Ma, J. Li, Y. Jiang, X. Wang, Improved photocatalytic activity of porous ZnO nanosheets by thermal deposition graphene-like g-C_3N_4 for CO_2 reduction with H_2O vapor, Appl. Surf. Sci. 509 (2020), 144773, https://doi.org/10.1016/j.apsusc.2019.144773.

[15] Y. Lin, Q. Wang, M. Ma, P. Li, V. Maheskumar, Z. Jiang, R. Zhang, Enhanced optical absorption and photocatalytic water splitting of g-C_3N_4/TiO_2 heterostructure through C&B codoping: A hybrid DFT study, Int. J. Hydrogen Energy. 46 (2021) 9417–9432, https://doi.org/10.1016/j.ijhydene.2020.12.114.

[16] J. Matos, J. Ocares-Riquelme, P.S. Poon, R. Montaña, X. García, K. Campos, J. C. Hernández-Garrido, M.M. Titirici, C-doped anatase TiO_2: Adsorption kinetics and photocatalytic degradation of methylene blue and phenol, and correlations with DFT estimations, J. Colloid Interface Sci. 547 (2019) 14–29, https://doi.org/10.1016/j.jcis.2019.03.074.

[17] C. Negi, P. Kandwal, J. Rawat, M. Sharma, H. Sharma, G. Dalapati, C. Dwivedi, Carbon-doped titanium dioxide nanoparticles for visible light driven photocatalytic activity, Appl. Surf. Sci. 554 (2021), 149553, https://doi.org/10.1016/j.apsusc.2021.149553.

[18] Q. Hou, W. Li, C. Li, X. Jia, C. Zhao, Effects of carbon doping and vacancy defect on the magnetism of anatase TiO_2, Phys. Lett. A. 383 (2019) 186–195, https://doi.org/10.1016/j.physleta.2018.10.028.

[19] Z. Gu, Z. Cui, Z. Wang, K. Sinkou Qin, Y. Asakura, T. Hasegawa, K. Hongo, R. Maezono, S. Yin, Intrinsic carbon-doping induced synthesis of oxygen vacancies-mediated TiO_2 nanocrystals: Enhanced photocatalytic NO removal performance and mechanism, J. Catal. 393 (2021) 179–189, https://doi.org/10.1016/j.jcat.2020.11.025.

[20] H. Heffner, R. Faccio, I. López–Corral, C–doped TiO_2(B): A density functional theory characterization, Appl. Surf. Sci. 551 (2021) 149479, https://doi.org/10.1016/j.apsusc.2021.149479.

[21] H. Gao, C. Ding, D. Dai, Density functional characterization of C-doped anatase TiO_2 with different oxidation state, J. Mol. Struct. THEOCHEM. 944 (2010) 156–162, https://doi.org/10.1016/j.theochem.2009.12.034.

[22] J. Sá, C. Garlisi, G. Palmisano, J. Czapla-Masztafiak, Y. Kayser, J. Szlachetko, Differences between bulk and surface electronic structure of doped TiO_2 with soft-elements (C, N and S), Mater. Chem. Phys. 208 (2018) 281–288, https://doi.org/10.1016/j.matchemphys.2018.01.041.

[23] W. Yuan, B. Zhu, X.-Y. Li, T.W. Hansen, Y. Ou, K.e. Fang, H. Yang, Z.e. Zhang, J. B. Wagner, Y.i. Gao, Y. Wang, Visualizing H 2 O molecules reacting at TiO 2 active sites with transmission electron microscopy, Science 367 (2020) 428–430.

[24] W. Yuan, Y. Wang, H. Li, H. Wu, Z.e. Zhang, A. Selloni, C. Sun, Real-Time Observation of Reconstruction Dynamics on TiO_2 (001) Surface under Oxygen via an Environmental Transmission Electron Microscope, Nano Lett. 16 (1) (2016) 132–137, https://doi.org/10.1021/acs.nanolett.5b03277.

[25] P.u. Guo, X. Fu, P. Deák, T. Frauenheim, J. Xiao, Activity and Mechanism Mapping of Photocatalytic NO_2 Conversion on the Anatase TiO_2 (101) Surface, J. Phys. Chem. Lett. 12 (32) (2021) 7708–7716, https://doi.org/10.1021/acs.jpclett.1c0226310.1021/acs.jpclett.1c02263.s001.

[26] G. Kresse, D. Joubert, From ultrasoft pseudopotentials to the projector augmented-wave method, Phys. Rev. B. 59 (3) (1999) 1758–1775, https://doi.org/10.1103/PhysRevB.59.1758.

[27] G. Kresse, J. Furthmüller, Efficient iterative schemes for ab initio total-energy calculations using a plane-wave basis set, Phys. Rev. B. 54 (16) (1996) 11169–11186, https://doi.org/10.1103/PhysRevB.54.11169.

[28] J.P. Perdew, A. Ruzsinszky, G.I. Csonka, O.A. Vydrov, G.E. Scuseria, L. A. Constantin, X. Zhou, K. Burke, Restoring the density-gradient expansion for exchange in solids and surfaces, Phys. Rev. Lett. 100 (13) (2008), https://doi.org/10.1103/PhysRevLett.100.136406.

[29] J.P. Perdew, K. Burke, M. Ernzerhof, Generalized Gradient Approximation Made Simple, Phys. Rev. Lett. 77 (18) (1996) 3865–3868, https://doi.org/10.1103/PhysRevLett.77.3865.

[30] S.L. Dudarev, G.A. Botton, S.Y. Savrasov, C.J. Humphreys, A.P. Sutton, Electron-energy-loss spectra and the structural stability of nickel oxide: An LSDA+U study, Phys. Rev. B. 57 (1998) 1505–1509, https://doi.org/10.1103/PhysRevB.57.1505.

[31] E. German, R. Faccio, A.W. Mombrú, Comparison of standard DFT and Hubbard-DFT methods in structural and electronic properties of TiO_2 polymorphs and H-titanate ultrathin sheets for DSSC application, Appl. Surf. Sci. 428 (2018) 118–123, https://doi.org/10.1016/j.apsusc.2017.09.141.

[32] E. German, R. Faccio, A.W. Mombrú, A DFT + U study on structural, electronic, vibrational and thermodynamic properties of TiO_2 polymorphs and hydrogen titanate: tuning the Hubbard ‘ U -term’, J. Phys. Commun. 1 (5) (2017) 055006, https://doi.org/10.1088/2399-6528/aa8573.

[33] S. Khan, H. Cho, D. Kim, S.S. Han, K.H. Lee, S.-H.-H. Cho, T. Song, H. Choi, Defect engineering toward strong photocatalysis of Nb-doped anatase TiO_2: Computational predictions and experimental verifications, Appl. Catal. B Environ. 206 (2017) 520–530, https://doi.org/10.1016/j.apcatb.2017.01.039.

[34] P. Mikrut, D. Mitoraj, R. Beranek, W. Macyk, Facet-dependent activity of tailored anatase TiO_2 crystals in photoanodes for photocatalytic fuel cells, Appl. Surf. Sci. 566 (2021) 150662, https://doi.org/10.1016/j.apsusc.2021.150662.

[35] C. Di Valentin, A. Selloni, Bulk and Surface Polarons in Photoexcited Anatase TiO_2, J. Phys. Chem. Lett. 2 (17) (2011) 2223–2228, https://doi.org/10.1021/jz2009874.

[36] C. Dette, M.A. Pérez-Osorio, S. Mangel, F. Giustino, S.J. Jung, K. Kern, Trellises of Molecular Oxygen on Anatase TiO_2 (101), J. Phys. Chem. C. 123 (43) (2019) 26170–26177, https://doi.org/10.1021/acs.jpcc.9b0431410.1021/acs.jpcc.9b04314.s001.

[37] D. Yu, W. Zhou, Y. Liu, B. Zhou, P. Wu, Density functional theory study of the structural, electronic and optical properties of C-doped anatase TiO_2 (101) surface, Phys. Lett. A. 379 (28-29) (2015) 1666–1670, https://doi.org/10.1016/j.physleta.2015.04.044.

[38] C. Chen, C. Zhao, X. Zhou, J. Chen, L. Chen, F. Li, DFT study on the interaction of H_2O and O_2 with α-Fe_2O_3 (001) surface, Vacuum. 188 (2021), 110164, https://doi.org/10.1016/j.vacuum.2021.110164.

[39] Z. Zhang, Z. Xiong, C. Zhao, P. Guo, H. Wang, Y. Gao, In-situ carbon-coated TiO_2 boosting the visible-light photocatalytic hydrogen evolution, Appl. Surf. Sci. 565 (2021), 150554, https://doi.org/10.1016/j.apsusc.2021.150554.
[40] A. Kupferer, A. Holm, A. Lotnyk, S. Mändl, S.G. Mayr, Compositional Patterning in Carbon Implanted Titania Nanotubes, Adv. Funct. Mater. n/a 31 (35) (2021) 2104250, https://doi.org/10.1002/adfm.202104250.
[41] Q. Wan, Y. Chen, S. Zhou, J. Lin, S. Lin, Selective hydrogenation of acetylene to ethylene on anatase TiO_2 through first-principles studies, J. Mater. Chem. A. 9 (24) (2021) 14064–14073, https://doi.org/10.1039/D1TA03490A.
[42] B.J. Morgan, G.W. Watson, Intrinsic n-type Defect Formation in TiO_2: A Comparison of Rutile and Anatase from GGA+ U Calculations, J. Phys. Chem. C. 114 (5) (2010) 2321–2328, https://doi.org/10.1021/jp9088047.
[43] J. Zhang, P. Zhou, J. Liu, J. Yu, New understanding of the difference of photocatalytic activity among anatase, rutile and brookite TiO_2, Phys. Chem. Chem. Phys. 16 (38) (2014) 20382–20386, https://doi.org/10.1039/C4CP02201G.
[44] R.A. Pawar, D.P. Dubal, S.V. Kite, K.M. Garadkar, V.M. Bhuse, Photoelectrochemical and photocatalytic activity of nanocrystalline TiO_2 thin films deposited by chemical bath deposition method, J. Mater. Sci. Mater. Electron. 32 (14) (2021) 19676–19687, https://doi.org/10.1007/s10854-021-06490-5.
[45] R. de L. Kronig, On the theory of dispersion of x-rays, Josa. 12 (1926) 547–557.
[46] H.A. Kramers, La diffusion de la lumiere par les atomes, in: Atti Cong. Intern. Fis. (Transactions Volta Centen. Congr. Como, 1927: pp. 545–557.
[47] C.E. Patrick, F. Giustino, GW quasiparticle bandgaps of anatase TiO_2 starting from DFT+U, J. Phys. Condens. Matter. 24 (20) (2012) 202201, https://doi.org/10.1088/0953-8984/24/20/202201.
[48] W. Ren, Z. Ai, F. Jia, L. Zhang, X. Fan, Z. Zou, Low temperature preparation and visible light photocatalytic activity of mesoporous carbon-doped crystalline TiO_2, Appl. Catal. B Environ. 69 (3-4) (2007) 138–144, https://doi.org/10.1016/j.apcatb.2006.06.015.
[49] N.U.M. Nor, N.A.S. Amin, Glucose precursor carbon-doped TiO_2 heterojunctions for enhanced efficiency in photocatalytic reduction of carbon dioxide to methanol, J. CO_2 Util. 33 (2019) 372–383, https://doi.org/10.1016/j.jcou.2019.07.002.
[50] Z. Shayegan, F. Haghighat, C.-S. Lee, Carbon-doped TiO_2 film to enhance visible and UV light photocatalytic degradation of indoor environment volatile organic compounds, J. Environ. Chem. Eng. 8 (2020), 104162, https://doi.org/10.1016/j.jece.2020.104162.
[51] R. Ragesh Nath, C. Nethravathi, M. Rajamathi, Hierarchically Porous, Biphasic, and C-Doped TiO_2 for Solar Photocatalytic Degradation of Dyes and Selective Oxidation of Benzyl Alcohol, ACS, Omega. 6 (18) (2021) 12124–12132, https://doi.org/10.1021/acsomega.1c0082510.1021/acsomega.1c00825.s001.